Orbital torque: Torque generation by orbital current injection

Dongwook Go [1,2,3] and Hyun-Woo Lee [1,*]

[1] *Department of Physics, Pohang University of Science and Technology, Pohang 37673, Korea*

[2] *Basic Science Research Institute, Pohang University of Science and Technology, Pohang 37673, Korea*

[3] *Peter Grünberg Institut and Institute for Advanced Simulation, Forschungszentrum Jülich and JARA, 52425 Jülich, Germany*

(Received 19 March 2019; revised manuscript received 23 January 2020; accepted 23 January 2020; published 20 February 2020)

We propose a mechanism of torque generation by injection of an orbital current, which we call *orbital torque*. In a magnetic bilayer consisting of a nonmagnet (NM) and a ferromagnet (FM), we consider a situation where the spin-orbit coupling (SOC) is present only in the FM. Although the SOC is absent in the NM, the orbital Hall effect can arise in the NM. When the resulting orbital Hall current is injected to the FM, the SOC of the FM converts the orbital angular momentum into spin, which exerts torque to the magnetization of the FM. Remarkably, even for small SOC strength comparable to that of $3d$ FMs, the orbital torque can be comparable to the spin torque induced by the spin Hall effect of the NM with strong SOC. This provides a way to experimentally probe the OHE and opens a venue to achieving spin-torque devices based on light elements that exhibit gigantic orbital response. Experimental implications are discussed.

DOI: 10.1103/PhysRevResearch.2.013177

I. INTRODUCTION

Spin injection into a ferromagnet (FM) generates a spin torque (ST) on local magnetic moments of the FM by the angular momentum transfer from the spin of injected conduction electrons. For ST generation, a spin current source is needed. A popular source is a nonmagnet (NM) with strong spin-orbit coupling (SOC), which exhibits sizable spin Hall effect (SHE). The ST of the SOC origin is called spin-orbit torque [1–20], which has drawn considerable attention as a powerful means to electrically control magnetic configuration such as current-induced magnetization switching [1–5] and domain wall motion [6–9].

Similar to the SHE, the orbital Hall effect (OHE) allows for electrical generation of a transverse orbital current. In transition metals, for example, electron wave functions near atomic cores have mainly d character, and superpositions such as $d_{zx} \pm i d_{yz}$ carry the orbital angular momentum (OAM) $L_z = \pm\hbar$. A flow of wave packets with such superposed wave functions generates an orbital current. Considering that an orbital current carries the angular momentum just like a spin current does, it is reasonable to expect that injection of an orbital current (or orbital injection in short) into a FM may generate a torque on local magnetic moments of the FM. We call such torque as *orbital torque* (OT), which provides an experimental way to detect the OHE. Although the OHE has not yet been experimentally verified, theoretical calculations [21,22] on $4d$ and $5d$ transition metals indicate that the orbital Hall conductivities (OHCs) of these NMs are about an order of magnitude larger than the spin Hall conductivities (SHCs). Moreover, our recent theoretical analysis finds that the OHC can be gigantic $\sigma_{\mathrm{OH}} \sim 10^4(\hbar/2|e|)(\Omega\mathrm{cm})^{-1}$ even in materials with negligible SOC [23,24]. Thus the OT also provides a venue to achieving high torque efficiency in spintronic devices.

In this paper, we explore the theoretical idea of the OT. By numerical calculation on a tight-binding model, we show that the OT can be sizable in magnetic bilayers consisting of NM and FM, even in a situation when the SOC of the NM is absent. This is attributed to highly efficient generation of the orbital current in the NM by the OHE. Thus, in light element systems in which the SOC is negligible, the OT is expected to be dominant over the ST.

Although conventional torque measurements (such as spin torque ferromagnetic resonance) measure the total sum of the OT and the ST, each individual torque can be distinguished as follows. In case of the ST, its sign and magnitude vary mainly with the choice of the NM and are affected much less by the choice of the FM. In particular, the sign of the ST cannot be flipped by the variation of the FM. In case of the OT, in contrast, depending on the choice of the FM its magnitude can vary significantly, and moreover its sign can also be flipped. We propose such FM dependence as a key feature for experimental verification of the OT. Moreover, we argue that unlike the ST the OT is drastically affected by the interface crystallinity, which originates in the nature of the orbital injection mechanism. This can be a way to disentangle the OT from the ST.

The rest of the paper is organized as follows. In Sec. II we introduce an overview on the mechanism of the OT. As a proof of the principle, Sec. III presents main results from the numerical calculation. In Sec. IV we discuss issues relevant

*hwl@postech.ac.kr

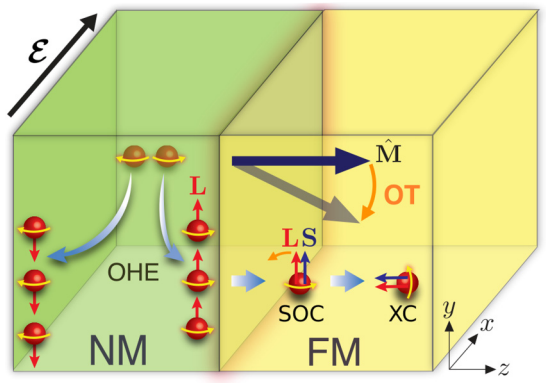

FIG. 1. Schematic illustration for the mechanism of the OT in a NM/FM bilayer. By an external electric field $\mathcal{E}$, the OHE occurs in the NM. Thus the OAM $\mathbf{L}$ is injected to the FM. The SOC of the FM then converts the injected $\mathbf{L}$ to the spin $\mathbf{S}$, which exerts torque on the magnetization $\hat{\mathbf{M}}$.

for the experimental detection of the OT. The conclusion of the paper is given in Sec. V.

II. MECHANISM

The mechanism of the OT consists of three steps. The first step is generation of the OAM or its current. For example, the OHE can be a way to generate the orbital current from the bulk [21–24]. Meanwhile, interfacial mechanisms such as orbital Rashba-Edelstein effect can also generate the OAM [25–31]. The second step is the orbital injection to the FM. In contrast to the spin injection, the orbital injection is critically affected by the interface crystallinity by the nature of its injection mechanism (see Sec. IV C for the discussion). The third step is conversion of the injected OAM to the spin, which interacts with the local magnetic moment by the exchange (XC) coupling and gives rise to the torque. Analogous to the ST, which originates in the spin injection, the OT is defined as a torque contribution arising from the orbital injection. As an illustration, Fig. 1 shows a schematics of the OT in the NM/FM bilayer, where the OHE occurs in the NM. When the SOC of the NM is zero, the SHE is absent but the OHE can still be gigantic [23]. The injected OAM is then converted to the spin by the SOC in the FM. In this case, the torque arises solely from the orbital injection and the thus resulting torque amounts to the OT.

III. RESULT

A. Tight-binding model

We investigate the OT in a NM/FM bilayer structure (Fig. 1). For a quantitative evaluation of the OT, we adopt the tight-binding description of the bilayer with $N_{\rm NM}(N_{\rm FM})$ atomic-layer-thick NM (FM), which is stacked along the $\hat{\mathbf{z}}$ direction [Fig. 2(a)]. We assume both NM and FM to have the simple cubic structure. The total Hamiltonian of the system can be formally expressed in $\mathbf{k}$ space as

$$H(\mathbf{k}) = \begin{pmatrix} H_{\rm NM}(\mathbf{k}) & T_{\rm int}^{\dagger}(\mathbf{k}) \\ T_{\rm int}(\mathbf{k}) & H_{\rm FM}(\mathbf{k}) \end{pmatrix}, \tag{1}$$

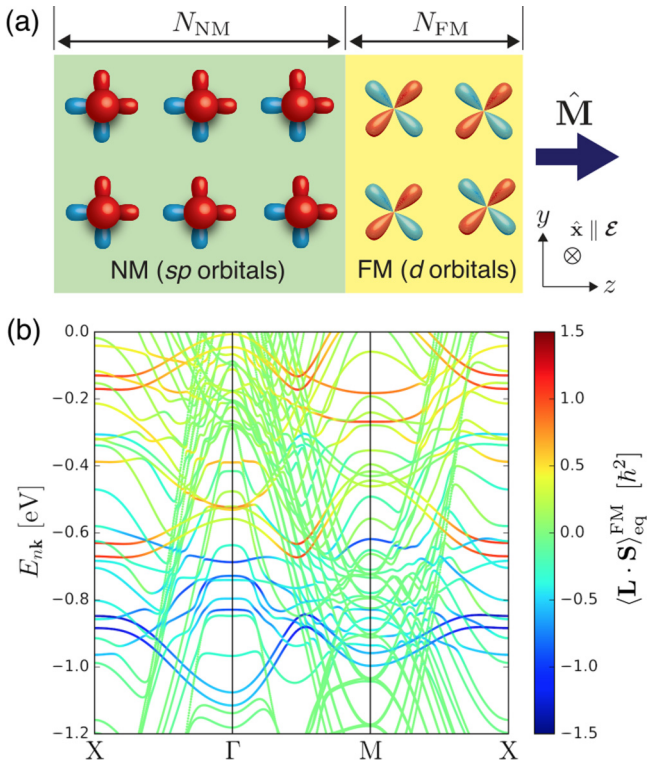

FIG. 2. (a) Schematic illustration of the tight-binding model of the NM/FM bilayer. (b) The band structure of the bilayer for $N_{\rm NM} = 8$ and $N_{\rm FM} = 2$. The color represents the equilibrium expectation value of the spin-orbit correlation in the FM region $\langle \mathbf{L}\cdot\mathbf{S}\rangle_{\rm eq}^{\rm FM}$ for each state.

where $\mathbf{k} = (k_x, k_y)$ is the crystal momentum, $H_{\rm NM(FM)}(\mathbf{k})$ describes the Hamiltonian in the NM(FM) sector of the bilayer, and $T_{\rm int}(\mathbf{k})$ describes the interfacial hoppings between the NM and FM. Details on the tight-binding model can be found in Appendix A.

Here we remark on a few important features of the model. For the NM, we adopt the sp model that has been used previously [23] to illustrate the OHE without the SOC. In this model, each lattice site can host s, p_x, p_y, and p_z orbitals, and the orbital hydridization, which is crucial for the emergence of the OHE [23], arises from the symmetry-allowed nearest-neighbor hoppings between s and $p_{x,y,z}$ orbitals. We neglect the SOC in the NM so that the SHE is absent. For the FM, we adopt a trivial d model; each lattice site can host d_{xy}, d_{yz}, d_{zx}, d_{z^2}, and $d_{x^2-y^2}$ orbitals with nearest-neighbor hoppings allowed. This d model does not allow any orbital hybridization, and thus there is no OHE [23,24]. In general, the OHE arises in more realistic d models that take into account one of the following complexities: next-nearest-neighbor hopping, extra orbitals (s or p), or non-simple-cubic structure. The d model is augmented by adding the SOC

$$H_{\rm so}^{\rm FM} = \frac{\alpha_{\rm so}^{\rm FM}}{\hbar^2}\mathbf{L}\cdot\mathbf{S} \tag{2}$$

and the XC coupling

$$H_{\rm xc}^{\rm FM} = \frac{J}{\hbar}\hat{\mathbf{M}}\cdot\mathbf{S}, \tag{3}$$

where $\hbar$ is the reduced Planck constant, $\mathbf{L}$ is the OAM operator, $\mathbf{S}$ is the spin operator, and $\hat{\mathbf{M}}$ denotes the magnetization direction of the FM. Here J and $\alpha_{\rm so}^{\rm FM}$ denote coupling strengths for the XC coupling and SOC, respectively. Below we focus on the case $\hat{\mathbf{M}} = \hat{\mathbf{z}}$. At the interface, the nearest-neighbor hoppings exist between the sp orbitals in the NM and the d orbitals in the FM.

All parameters of the NM and FM are set to have typical energy scales of nonmagnetic and magnetic metals. In particular, we set $\alpha_{\rm so}^{\rm FM} = 100$ meV, which is a typical SOC strength of $3d$ transition metals [24,31,32]. We emphasize that the nonzero $\alpha_{\rm so}^{\rm FM}$ is crucial for the OT since $\hat{\mathbf{M}}$ couples only to $\mathbf{S}$ and there is no direct coupling between $\hat{\mathbf{M}}$ and $\mathbf{L}$ in the Hamiltonian. Thus for the injected OAM to generate the OT, it should be first converted to spin through the SOC and then the resulting spin can generate the torque through the XC coupling as illustrated in Fig. 1.

Figure 2(b) shows the band structure of the NM/FM bilayer for $N_{\rm NM} = 8$ and $N_{\rm FM} = 2$, where the color represents the equilibrium expectation value of the spin-orbit correlation in the FM region $\langle \mathbf{L}\cdot\mathbf{S}\rangle_{\rm eq}^{\rm FM}$ for each state. The correlation is negative in the lower energy range (-1.1 eV $< E_{n\mathbf{k}} <$ -0.7 eV) and positive in the higher energy range (-0.3 eV $< E_{n\mathbf{k}} < +0.2$ eV). In the middle energy range (-0.7 eV $< E_{n\mathbf{k}} < -0.3$ eV), states with positive and negative correlations coexist. In Sec. III E we demonstrate that the sign of $\langle \mathbf{L}\cdot\mathbf{S}\rangle_{\rm eq}^{\rm FM}$ is crucial for the determination of sign of the OT.

B. Kubo formula

For the calculation of the OT and related responses such as OAM, spin, and their currents, we employ the Kubo formula within the linear response theory. A response of an observable $\mathcal{O}$ by an external electric field $\boldsymbol{\mathcal{E}} = \mathcal{E}_x\hat{\mathbf{x}}$ is given by the sum of the intraband and interband contributions

$$\langle\mathcal{O}\rangle = \langle\mathcal{O}\rangle^{\rm intra} + \langle\mathcal{O}\rangle^{\rm inter} \tag{4}$$

under the relaxation time approximation, which assumes constant broadening of the energy spectrum by Γ that corresponds to the characteristic relaxation time $\tau = \hbar/2\Gamma$. The intraband contribution

$$\langle\mathcal{O}\rangle^{\rm intra} = \sum_{n\mathbf{k}}[f_{n\mathbf{k}+\Delta\mathbf{k}} - f_{n\mathbf{k}}]\,\langle u_{n\mathbf{k}}|\,\mathcal{O}(\mathbf{k})\,|u_{n\mathbf{k}}\rangle \tag{5a}$$

$$\approx -e\mathcal{E}_x\tau\sum_{n\mathbf{k}}\frac{\partial f_{n\mathbf{k}}}{\partial E_{n\mathbf{k}}}\,\langle u_{n\mathbf{k}}|\,\mathcal{O}(\mathbf{k})\,|u_{n\mathbf{k}}\rangle\,\langle u_{n\mathbf{k}}|\,v_x(\mathbf{k})\,|u_{n\mathbf{k}}\rangle \tag{5b}$$

arises due to shift of the Fermi-Dirac distribution function $f_{n\mathbf{k}}$ by $\Delta\mathbf{k} = -e\boldsymbol{\mathcal{E}}\tau/\hbar$. Here $e > 0$ is the unit charge, $v_x(\mathbf{k}) = (1/\hbar)(\partial H(\mathbf{k})/\partial k_x)$ is the velocity operator along the $\hat{\mathbf{x}}$ direction, $|u_{n\mathbf{k}}\rangle$ is a periodic part of the Bloch state, and $E_{n\mathbf{k}}$ is the corresponding energy eigenvalue. For any arbitrary operator $\mathcal{C}$, we define $\mathcal{C}(\mathbf{k}) = e^{-i\mathbf{k}\cdot\mathbf{r}}\mathcal{C}e^{i\mathbf{k}\cdot\mathbf{r}}$ in $\mathbf{k}$ space. On the other hand, the interband contribution

$$\langle\mathcal{O}\rangle^{\rm inter} = e\hbar\mathcal{E}_x\sum_{nm\mathbf{k}}(f_{n\mathbf{k}} - f_{m\mathbf{k}}) \times {\rm Im}\left[\frac{\langle u_{n\mathbf{k}}|\,\mathcal{O}(\mathbf{k})\,|u_{m\mathbf{k}}\rangle\,\langle u_{m\mathbf{k}}|\,v_x(\mathbf{k})\,|u_{n\mathbf{k}}\rangle}{(E_{n\mathbf{k}} - E_{m\mathbf{k}} + i\Gamma)^2}\right] \tag{6}$$

arises due to change of the quantum state by coherent superpositions for each $\mathbf{k}$. In the relaxation time approximation, disorder scatterings are incorporated in a semiclassical manner; while the electronic structure is quantum mechanically treated, scattering and relaxation of the electron are treated by introducing the level broadening Γ. For example, the vertex-correction effect is not captured in this approach. Below throughout the paper, we assume $\Gamma = 25$ meV, which is a room temperature scale.

Based on the Kubo formula expressions in Eqs. (5) and (6), we evaluate responses of the OAM, spin, and their currents at each atomic layer located at z. The operators of the OAM and spin are locally defined as

$$\mathbf{X}(z) = P(z)\mathbf{X}P(z) \tag{7}$$

for $\mathbf{X} = \mathbf{L}$ or $\mathbf{S}$, where $P(z)$ is the projection operator to the atomic layer at z. The z component of the current for $\mathbf{X}$, which is relevant for the orbital and spin injection, is defined as

$$j_z^{\mathbf{X}}(z) = \tfrac{1}{2}\{v_z, \mathbf{X}(z)\}, \tag{8}$$

where the velocity operator along the z direction is defined as

$$v_z = \frac{1}{i\hbar}\sum_{zz'}(z - z')P(z)H(\mathbf{k})P(z'). \tag{9}$$

C. Definition of the OT

Although the origin of the OT is the orbital injection, torque acting in the magnetization is proportional to the spin, which is converted from the injected OAM. Thus, the torque $\mathbf{T}$ acting on the FM can be obtained from spin accumulation as

$$\mathbf{T} = \frac{J}{\hbar}\hat{\mathbf{M}}\times\langle\mathbf{S}\rangle^{\rm FM}, \tag{10}$$

where $\langle\mathbf{S}\rangle^{\rm FM} = \sum_{z\in{\rm FM}}\langle\mathbf{S}(z)\rangle$ is the spin accumulation in the FM. When $\langle\mathbf{S}\rangle^{\rm FM}$ originates from the injected OAM, $\mathbf{T}$ amounts to the OT.

Analogous to the ST, in the lowest order of $\hat{\mathbf{M}}$ (or rotation symmetry in the xy plane is assumed, i.e., a polycrystalline sample) the OT can be decomposed into fieldlike and dampinglike components:

$$\mathbf{T} = \tau_{\rm f}\hat{\mathbf{M}}\times\hat{\mathbf{y}} + \tau_{\rm d}\hat{\mathbf{M}}\times(\hat{\mathbf{M}}\times\hat{\mathbf{y}}), \tag{11}$$

where $\tau_{\rm f(d)}$ refers to the fieldlike (dampinglike) component of the OT. This is similar to the generation of the fieldlike and dampinglike STs when a spin current polarized along $\hat{\mathbf{y}}$ direction is injected into a FM magnetized along the $\hat{\mathbf{z}}$ direction [14]. For instance, when $\hat{\mathbf{M}} = \hat{\mathbf{z}}$, which is assumed in the tight-binding model, $\tau_{\rm f} = (J/\hbar)\langle S_y\rangle^{\rm FM}$ and $\tau_{\rm d} = -(J/\hbar)\langle S_x\rangle^{\rm FM}$. We find that $\langle S_y(z)\rangle$ and $\langle S_x(z)\rangle$ arise from the intraband [Eq. (5)] and interband [Eq. (6)] contributions, respectively. Thus the fieldlike (dampinglike) OT is odd (even) under sign reversal of $\hat{\mathbf{M}}$.

D. Orbital/spin response under orbital Hall current injection

We evaluate the electric field responses for the OAM, spin, and their currents by using the Kubo formula within the relaxation time approximation, as described in Sec. III B. For the calculation, we assume $N_{\rm NM} = 20$ and $N_{\rm FM} = 10$;

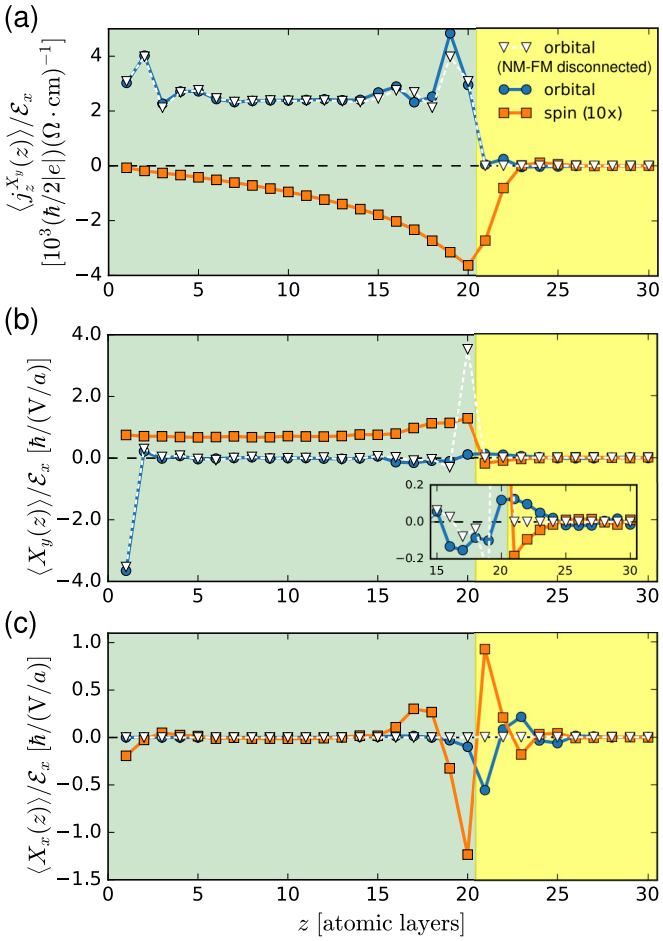

FIG. 3. (a) $\langle j_z^{X_y}(z)\rangle/\mathcal{E}_x$, (b) $\langle X_y(z)\rangle/\mathcal{E}_x$, and (c) $\langle X_x(z)\rangle/\mathcal{E}_x$ as a function of z for $E_F = -0.9$ eV. Here $\mathbf{X} = \mathbf{L}$ or $\mathbf{S}$. Blue circles and orange squares depict the orbital and spin, respectively. White inverted triangles depict the orbital when the NM and FM are disconnected. The NM ($1 \leqslant z \leqslant 20$) and the FM ($21 \leqslant z \leqslant 30$) regions are colored in green and yellow, respectively. The inset in (b) presents a magnified plot near the NM/FM interface.

thus the NM and the FM are located at $1 \leqslant z \leqslant 20$ and $21 \leqslant z \leqslant 30$, respectively. We present the result for the Fermi energy $E_F = -0.9$ eV. In Fig. 3, white inverted triangles indicate the response for the orbital when the NM and FM are disconnected, *viz.* $T_{\rm int}(\mathbf{k}) = 0$ in Eq. (1). Blue circles and orange squares represent the responses for the orbital and spin, respectively, when the NM and FM are connected. Note that responses for the spin are $10\times$ enlarged.

We first consider the case where the NM and FM are disconnected. For the orbital Hall current [Fig. 3(a)], it exhibits symmetric distribution within the NM. On the other hand, there is no response in the FM since the FM is disconnected from the NM and the OHE within the FM itself is assumed to be absent. We find that the OHC in the NM is more than 2000 $(\hbar/2|e|)(\Omega\cdot\mathrm{cm})^{-1}$, which is gigantic. This agrees with the previous calculation of the OHC in the periodic structure [23]. The spin Hall current is absent in both NM and FM when the NM and FM are disconnected (not shown). In Fig. 3(b) we find that $\langle L_y(z)\rangle$ exhibits asymmetric distribution and finite accumulation at the edges ($z = 1$ and 20) in the NM. This result can be interpreted as the orbital accumulation at the edges due to the OHE in the NM. Such orbital accumulation is zero in the FM due to absence of the OHE. Since the SHE is absent in both NM and FM, $\langle S_y(z)\rangle$ is absent in both NM and FM. On the other hand, $\langle L_x(z)\rangle$ is zero when the NM and FM are disconnected [Fig. 3(c)]. In the NM, it is because this requires breaking of the time-reversal symmetry. Even though the time-reversal symmetry is broken in the FM, $\langle L_x(z)\rangle$ is zero due to absence of the OHE and SHE. For the same reason, $\langle S_x(z)\rangle$ is also zero (not shown).

Once the NM and FM are connected, part of the orbital Hall current is injected to the FM, which is converted to the spin Hall current by the SOC of the FM [Fig. 3(a)]. We also find the spin Hall current in the NM region, which is decaying from the interface [Fig. 3(a)]. This is because reflected current from the interface becomes spin-polarized by the SOC in the FM [Eq. (2)]. Even though the SOC is absent in the NM, the decay of the reflected spin current is observed due to finite Γ. Figure 3(b) shows spatial profiles of $\langle L_y(z)\rangle$ and $\langle S_y(z)\rangle$. Near $z = 1$, which is far from the NM/FM interface, $\langle L_y(z)\rangle$ remains essentially unchanged. Near the interface ($z = 20$), on the other hand, $\langle L_y(z)\rangle$ is reduced significantly since the orbital Hall current is now injected into the FM instead of getting accumulated at the interface. The injected orbital in the FM produces not only $\langle L_y(z)\rangle$ but also $\langle S_y(z)\rangle$ due to the SOC [Eq. (2)]. By the way, the spin accumulation in the NM is due to partial reflection of the orbital Hall current from the NM/FM interface, which becomes spin-polarized by the SOC [Eq. (2)].

As $\langle S_y(z)\rangle$ becomes nonzero in the FM, the spin precesses around $\hat{\mathbf{M}}$ due to the XC coupling [Eq. (3)] and produces $\langle S_x(z)\rangle$ as well [Fig. 3(c)]. This precession results in oscillatory profiles of $\langle S_y(z)\rangle$ and $\langle S_x(z)\rangle$ in the FM, which resemble oscillatory spin accumulation profiles [14] in a conventional situation, where a *spin* current is injected into a FM to generate the ST. The oscillatory profiles of $\langle S_x(z)\rangle$ and $\langle S_y(z)\rangle$ in the FM are accompanied by similar oscillatory profiles of $\langle L_x(z)\rangle$ and $\langle L_y(z)\rangle$. The coexistence of the spin and orbital accumulation oscillations is due to the SOC, and we note that the spin and orbital oscillations are 180° out of phase [Figs. 3(b) and 3(c)], which we attribute to negative spin-orbit correlation $\langle\mathbf{L}\cdot\mathbf{S}\rangle_{\rm eq}^{\rm FM}$ at $E_F = -0.9$ eV [Fig. 2(b)].

E. What determines the sign of the OT?

Since τ_d plays a more important role for the current-induced magnetization dynamics than τ_f [2,3], we focus on $\langle S_x\rangle^{\rm FM}$. Figure 4(a) shows that the ratio $\langle S_x\rangle^{\rm FM}/\mathcal{E}_x$ (orange squares) is positive for -1.0 eV $\lesssim E_F \lesssim -0.6$ eV and negative for -0.2 eV $\lesssim E_F \lesssim 0.0$ eV. For comparison, the ratio $\langle L_x\rangle^{\rm FM}/\mathcal{E}_x$ (blue circles) is also shown, where $\langle L_x\rangle^{\rm FM} \equiv \sum_{z\in{\rm FM}}\langle L_x(z)\rangle$. Note that the relative ratio between $\langle S_x\rangle^{\rm FM}$ and $\langle L_x\rangle^{\rm FM}$ is negative for -1.0 eV $\lesssim E_F \lesssim -0.6$ eV, and positive for -0.2 eV $\lesssim E_F \lesssim 0.0$ eV. The E_F dependence of the relative ratio sign closely resembles the energy dependence of the spin-orbit correlation $\langle\mathbf{L}\cdot\mathbf{S}\rangle_{\rm eq}^{\rm FM}$ in Fig. 2(b). By combining the calculation result in Fig. 4(a) with the fact that the OHC of the NM is positive essentially for all E_F [23], we find that the sign of $\langle S_x\rangle^{\rm FM}/\mathcal{E}_x$ tends to be determined by the sign of the product between the OHC of the NM and the spin-orbit

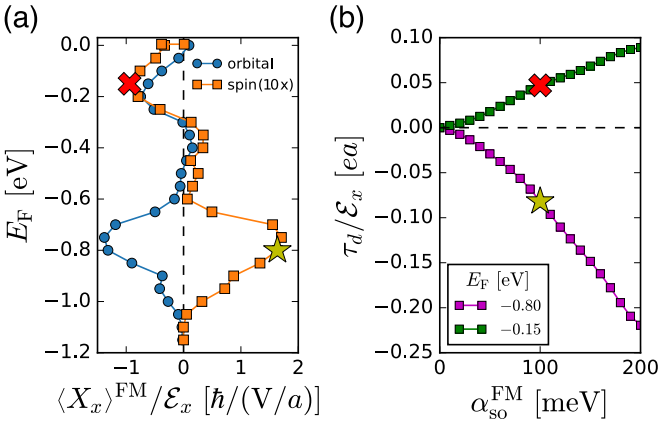

FIG. 4. (a) $\langle S_x\rangle^{FM}/\mathcal{E}_x$ (orange squares for 10× magnified values) as a function of E_F with $\alpha_{so}^{FM} = 100$ meV. For comparison, $\langle L_x\rangle^{FM}/\mathcal{E}_x$ (blue circles) is also shown. (b) $\tau_d/\mathcal{E}_x$ as a function of α_{so}^{FM} with $E_F = -0.80$ eV (purple squares) and $E_F = -0.15$ eV (green squares). The yellow star and red cross symbols in (a) and (b) are obtained for the same E_F and α_{so}^{FM}. For this calculation, smaller system size is used ($N_{NM} = 8$ and $N_{FM} = 2$).

correlation in the FM. Considering that $\langle S_x\rangle^{FM}$ determines the dampinglike OT, the latter tendency may be regarded as the OT counterpart of the sign "rule" for the ST; the dampinglike ST tends to be determined by the sign of the spin Hall conductivity (SHC) in the NM [2,3,14]. Meanwhile, the fieldlike OT exhibits more complicated behavior, which sensitively depends on the electronic structure, because it originates in an interfacial mechanism such as orbital Rashba-Edelstein effect, analogous to the fieldlike ST, which is dominantly governed by an interfacial mechanism from the Rashba-type states [18].

F. How large is the OT?

Figure 4(b) shows the ratio $\tau_d/\mathcal{E}_x$ as a function of α_{so}^{FM} for $E_F = -0.80$ eV (purple squares) and $E_F = -0.15$ eV (green squares). These two E_F values are close to the peak positions in Fig. 4(a) (denoted by the yellow star and the red cross). For these favorable choices of E_F, values of $\tau_d/\mathcal{E}_x$ are -0.08 *ea* and $+0.05$ *ea* for $\alpha_{so}^{FM} = 100$ meV, which is the SOC energy scale for 3*d* FMs. Here *a* is the lattice constant, which is set to 5 Å. By increasing α_{so}^{FM}, they reach up to -0.22 *ea* and $+0.09$ *ea* for $\alpha_{so}^{FM} = 200$ meV, which is the SOC energy scale for 4*d* transition metals. Note that these values $\tau_d/\mathcal{E}_x \sim 0.1$ *ea* for $\alpha_{so}^{FM} = 100,\ 200$ meV are not negligible compared to the corresponding value ∼0.5 *ea* for the dampinglike torque calculated for the Pt/Co bilayer [18,20] with the SOC strength of 500 meV for Pt. Then, considering that the OHC in real materials such as V is gigantic $\sigma_{OH} \sim 12\,000\ (\hbar/2|e|)(\Omega\cdot\mathrm{cm})^{-1}$, which is about six times larger than the OHC of the *sp* model used in our calculation, $\tau_d/\mathcal{E}_x$ for real NMs may be proportionally larger and comparable to the corresponding ST value for the Pt/Co bilayer. Although quantitative predictions for $\tau_d/\mathcal{E}_x$ require realistic calculations that take material details into account, we argue it is still reasonable to expect that the OT may be sizable for a FM with weak SOC, thus providing an alternative route to enhancing the torque efficiency.

TABLE I. Relative signs of the OT and ST depending on the spin-orbit correlations in the NM and FM.

	$\langle\mathbf{L}\cdot\mathbf{S}\rangle_{eq}^{FM} > 0$	$\langle\mathbf{L}\cdot\mathbf{S}\rangle_{eq}^{FM} < 0$
$\langle\mathbf{L}\cdot\mathbf{S}\rangle_{eq}^{NM} > 0$	Same sign	Opposite signs
$\langle\mathbf{L}\cdot\mathbf{S}\rangle_{eq}^{NM} < 0$	Opposite signs	Same sign

IV. DISCUSSION

A. Disentangling the OT from the ST

So far we have assumed that the SOC is absent in the NM. However, in general, the SOC exists in the NM and both the OT and ST contribute to the torque. Here we discuss competition between the OT and ST and how to disentangle them. When the SOC is present in the NM, part of the orbital current is converted to the spin current and the SHE follows the OHE [21–23]. Thus, on top of the OT, injection of the spin Hall current into the FM generates the ST. It is known that OHE and SHE occur in the same (opposite) direction if $\langle\mathbf{L}\cdot\mathbf{S}\rangle_{eq}^{NM}$ is positive (negative) at E_F [21–23]. Thus, when $\langle\mathbf{L}\cdot\mathbf{S}\rangle_{eq}^{FM} > 0$ at E_F, which is a case for Ni, the OT and ST add up if $\langle\mathbf{L}\cdot\mathbf{S}\rangle_{eq}^{NM} > 0$ and cancel each other if $\langle\mathbf{L}\cdot\mathbf{S}\rangle_{eq}^{NM} < 0$. This situation becomes the opposite when $\langle\mathbf{L}\cdot\mathbf{S}\rangle_{eq}^{FM} < 0$, as in Gd. This is summarized in Table I.

This implies that when the OT and the ST add up, the total torque may go even beyond the level expected from the theoretical value for the SHC of a NM, as in recent experiments [33,34]. When the OT and ST cancel each other, the total torque may even exhibit the opposite sign compared to the sign expected from the SHC of the NM. For example, Ta and W are candidate systems where such sign reversal may be realized since the OHC is of opposite sign and much larger than the SHC in these materials [21].

Unfortunately, the OT and ST exhibit *qualitatively* similar behavior, and thus disentangling the OT from the ST is challenging. The orbital and spin operator transform in the same way for symmetry operations, i.e., both OT and ST exhibit the same angular dependence. Nonetheless, the OT and ST are expected to exhibit different *quantitative* features. One characteristic feature of the OT is its strong correlation with $\langle\mathbf{L}\cdot\mathbf{S}\rangle_{eq}^{FM}$ as demonstrated in Figs. 2(b) and 4(a). This suggests that the OT can be probed through material variation of a FM. This is in stark contrast to the ST, where the role of the FM is less important. This behavior can be systematically studied by controlling the stoichiometry of the FM alloys.

Phenomenologically, the *effective* spin Hall conductivity obtained from the torque measurement may be expressed as

$$\sigma_{SH}^{eff} = T_S\sigma_{SH}^{NM} + T_O\sigma_{OH}^{NM}\xi_{so}^{FM}, \tag{12}$$

where $\sigma_{SH(OH)}^{NM}$ is the OHC (SHC) of the NM, $T_{S(O)}$ is spin (orbital) transparency at the interface, and ξ_{so}^{FM} is the conversion ratio from the orbital to spin in the FM, which is proportional to $\langle\mathbf{L}\cdot\mathbf{S}\rangle_{eq}^{FM}$. Here the first term in the right-hand side of Eq. (12) corresponds to the ST contribution and the second term corresponds to the OT contribution.

In the above discussion, the SHC in the FM is ignored. However, the SOC in the FM may result in a self-induced torque due to sizable SHE in the FM, as pointed out in

Refs. [35,36]. The SHE in the FM leads to an antisymmetric accumulation of the spin within the FM layer, leading to a nonuniform tilting of the magnetization. Thus, when the thickness of the FM is smaller than the spin diffusion length, this effect is expected to be small. On the other hand, in the mechanism of the OT, transient OAM and spin in the FM exhibit exponential decay from the NM/FM interface, as shown in Fig. 3. Therefore, measuring the dependence of the torque on the FM thickness may distinguish the spin accumulation induced by the SHE of the FM and the spin accumulation induced by the orbital injection from the NM.

B. Onsager's reciprocity: Orbital pumping

The OT describes a response of the torque and resulting magnetization dynamics induced by orbital current injection. The Onsager's reciprocal relations guarantee the existence of a reciprocal process of the OT: pumping of the orbital current by the magnetization dynamics. We denote this phenomenon orbital pumping (OP) in analogy to the spin pumping (SP). Because of the SOC in the FM, both the spin and orbital are pumped by the magnetization dynamics. Depending on the spin-orbit correlation of the FM $\langle \mathbf{L}\cdot\mathbf{S}\rangle_{\rm eq}^{\rm FM}$, the sign of the OP can be same or opposite to the sign of the SP.

In the NM/FM bilayer, pumped orbital and spin are converted to the charge current by the inverse OHE (IOHE) and inverse SHE (ISHE) in the NM, respectively. While the IOHE does not require the SOC for the same reason as the OHE does not require the SOC, the ISHE requires the SOC. Thus when the SOC in the NM is negligible, leading contribution of the *effective* ISHE voltage comes from the IOHE. When the SOC is appreciable in the NM, the relative sign of the IOHE and ISHE is determined by the spin-orbit correlation of the NM, $\langle \mathbf{L}\cdot\mathbf{S}\rangle_{\rm eq}^{\rm NM}$. This kind of reciprocal process is captured by the tight-binding model used in the calculation of the OT (Fig. 2).

Therefore when the magnetization precesses, there are two channels for generating the effective ISHE voltage: (1) the OP followed by the IOHE and (2) the SP followed by the ISHE. The channels (1) and (2) are governed by $\langle \mathbf{L}\cdot\mathbf{S}\rangle_{\rm eq}^{\rm FM}$ and $\langle \mathbf{L}\cdot\mathbf{S}\rangle_{\rm eq}^{\rm NM}$, respectively. Whether the two channels contribute in the same sign or opposite signs of the voltage is analogous to the relation between the OT and ST, following the relation in Table I. The magnitudes of the contributions (1) and (2) are expected to be comparable.

C. Role of the interface crystallinity

Another feature of the OT distinct from the ST is its dependence on the interface crystallinity. For injection of the OAM across the interface, it must occur through orbital hybridizations at the NM/FM interface. In the tight-binding model in Fig. 2(a), interfacial hoppings

$$\gamma_{pd}^{\sigma} = \left\langle p_z^{\rm NM}\right| H_{\rm hop} \left|d_{z^2-x^2}^{\rm FM}\right\rangle, \tag{13a}$$

$$\gamma_{pd}^{\pi} = \left\langle p_x^{\rm NM}\right| H_{\rm hop} \left|d_{zx}^{\rm FM}\right\rangle \tag{13b}$$

are crucial for transferring $\langle L_y\rangle$ between the NM an the FM. Once a state carrying finite OAM, $|L_y^{(p)}=\pm1\rangle = |p_z\rangle \pm i\,|p_x\rangle$, for example, is induced in the NM, the interface hoppings in Eq. (13) can generate a state $|L_y^{(d)}=\pm2\rangle = |d_{z^2-x^2}^{\rm FM}\rangle \pm i\,|d_{zx}^{\rm FM}\rangle$ that also carries OAM. It can be shown that when the relative sign of $\gamma_{pd\sigma}$ and $\gamma_{pd\pi}$ is flipped, the sign of the OT changes (see Appendix B). Thus even spin-conserving interface scatterings can result in orbital relaxation, making the *orbital transparency* $T_{\rm O}$ more sensitive to the interface crystallinity than the spin transparency $T_{\rm S}$ [Eq. (12)]. The interface crystallinity may be varied in experiments by different sample preparation methods.

Interface crystallinity can also differ depending on chemical properties of the NM and FM atoms. For example, when the NM and FM elements tend to be mixed, interdiffusion of the NM and FM elements forms a mixed layer. This can suppress the OT since the atomic ordering of the NM and FM atoms disappears at the interface. On the other hand, when the NM and FM elements do not mix, a sharp interface is maintained, which is favorable for the OT. Note that the atomic ordering persists locally even in polycrsytalline samples.

D. Material systems

Light element systems are promising candidates that are expected to have dominant OT contribution in the current-induced magnetization dynamics, i.e., the NM/FM bilayer shown in Fig. 1. This is advantageous for unambiguously quantifying the OT since the ST is negligible. Current-induced magnetization switching has been realized in a Zr/CoFeB bilayer, in which heavy element is absent [37]. According to theoretical calculation on the hcp Zr, the OHC $\sigma_{\rm OH} \approx +5300\ (\hbar/|e|)(\Omega{\rm cm})^{-1}$ is about 30 times larger than the SHC $\sigma_{\rm SH} \approx -170\ (\hbar/|e|)(\Omega{\rm cm})^{-1}$ [37]. Thus it is possible that the OT is in action for the torque generation.

In the past, unexpectedly large signals have been measured in Cr [38,39] and Py [40,41] systems from the SP experiment. We remark that the effective ISHE voltage measured from the experiment is the sum of the two independent contributions (1) and (2) (see Sec. IV B). On the experiment in Ref. [38], which studied the variation of the effective spin Hall angle as a function of atomic number Z among $3d$ transition metals, Fig. 3(b) of Ref. [38] shows that the sign is negative for $Z =$ 22–25 and positive for $Z =$ 26–29. This Z-dependent sign variation seems to indicate that the channel (2) is probably more important for this particular experiment. However, we note that the measured effective ISHE does not quantitatively agree well with the theoretical estimation [24]. This implies that the signal from channel (1) contributes together with channel (2). We suggest that the variation of not only the NM material choice but also the variation of the FM material choice can provide more information on the role of the IOHE.

Alloying provides a systematic way of tuning the spin-orbit correlation. For example, we expect that alloying a FM with heavy elements would not only increase the OT contribution since the conversion becomes more effective as $\xi_{\rm so}^{\rm FM}$ grows but also provide a way to systematically investigate the competition between the ST and the OT [Eq. (12)]. Although majority of the current-induced torque experiments employ transition metals, we emphasize that combining d orbital and p orbital elements may open a venue for achieving desirable material properties. Among different classes of alloys, Heusler alloys are interesting in that they exhibit various kinds of nonmagnetic and magnetic phases [42]. Recently,

CoGa has been proposed to have large SHC by the *pd* hybridization [43]. Because the orbital hybridization is crucial for the emergence of the OHE [23,24], we compare the value of the OHC and SHC in CoGa from first-principles calculation [44]. We find that the OHC is indeed gigantic, $\sigma_{\rm OH} \approx +2770\ (\hbar/|e|)(\Omega{\rm cm})^{-1}$, which is almost 20 times larger than the SHC $\sigma_{\rm SH} \approx 136\ (\hbar/|e|)(\Omega{\rm cm})^{-1}$. This implies that if more than 5% of the injected orbital is converted to the spin in the adjacent FM, the OT contribution is larger than the ST contribution.

Another interesting class of materials is two-dimensional systems such as transition metal dichalcogenide, in which *p* and *d* orbital characters coexist. Recently, it has been theoretically found that orbital Hall insulating phase can be realized in two-dimensional systems [45,46]. This may ignite research on two-dimensional materials as orbital current generators for the OT device applications.

Finally we also remark that the OAM can be generated not only by the OHE but also by the interfacial Rashba-type states with chiral OAM textures [25–29,31]. Recently Ref. [47] claimed that large dampinglike torque measured in $Pt/Co/SiO_2$ is correlated with the pronounced orbital splitting of Co states due to asymmetrical hybridization with Pt and SiO_2. Meanwhile, sizable fieldlike torque was measured in $Py/(Cu)/AlO_x$ structure [48]. Since the SOC is negligible in this structure, the fieldlike torque could be due to orbital Rashba states.

V. CONCLUSION

In conclusion, we propose a mechanism of torque generation by the orbital injection, called the OT. In a NM/FM bilayer, the OHE arises in the NM even without the SOC, by which the OAM can be injected to the FM. In the FM, the injected OAM is converted to the spin by the SOC and exerts torque to the magnetization of the FM. Remarkably, we find that even for small SOC strength of the FM comparable to that of 3*d* FMs, the OT can be comparable to the ST induced by the spin Hall effect of the NM with strong SOC. For disentangling the OT from the ST, we propose variations of the FM kind and interface crystallinity. The OT not only provides a way to experimentally probe the OHE but also opens a new venue to achieving spin-torque devices based on light elements that exhibit gigantic orbital response.

ACKNOWLEDGMENTS

We acknowledge Daegeun Jo, Kyung-Jin Lee, Junyeon Kim, YoshiChika Otani, Jan-Philipp Hanke, Frank Freimuth, and Yuriy Mokrousov for insightful discussions. D.G. and H.-W.L. were supported by the Samsung Science and Technology Foundation (Grant No. BA-1501-07).

APPENDIX A: TIGHT-BINDING MODEL

The tight-binding model for a magnetic bilayer presented in this paper is composed of a NM layer and a FM layer. The numbers of layers for the NM and the FM are $N_{\rm NM}$ and $N_{\rm FM}$, respectively. We assume the simple cubic structure for both NM and FM with only nearest-neighbor hoppings allowed. We also assume that the layer is periodic in x and y directions, and the layers are stacked along the z direction. Thus, the NM is located from $z = 1$ to $z = N_{\rm NM}$, and the FM is located from $z = N_{\rm NM} + 1$ to $z = N_{\rm NM} + N_{\rm FM}$ (in unit of the lattice spacing a), and we use the Bloch theorem for x and y directions by introducing the crystal momentum $\mathbf{k} = (k_x, k_y)$. The total Hamiltonian is formally written as

$$H(\mathbf{k}) = \left(\begin{array}{ccccc|ccccc}
H_{\rm 2d}^{\rm NM}(\mathbf{k}) & T^{\rm NM\dagger} & \cdots & 0 & 0 & 0 & 0 & \cdots & 0 & 0 \\
T^{\rm NM} & H_{\rm 2d}^{\rm NM}(\mathbf{k}) & \cdots & 0 & 0 & 0 & 0 & \cdots & 0 & 0 \\
\vdots & \vdots & \ddots & \vdots & \vdots & \vdots & \vdots & \ddots & \vdots & \vdots \\
0 & 0 & \cdots & H_{\rm 2d}^{\rm NM}(\mathbf{k}) & T^{\rm NM\dagger} & 0 & 0 & \cdots & 0 & 0 \\
0 & 0 & \cdots & T^{\rm NM} & H_{\rm 2d}^{\rm NM}(\mathbf{k}) & T_{\rm int}^{\dagger} & 0 & \cdots & 0 & 0 \\
\hline
0 & 0 & \cdots & 0 & T_{\rm int} & H_{\rm 2d}^{\rm FM}(\mathbf{k}) & T^{\rm FM\dagger} & \cdots & 0 & 0 \\
0 & 0 & \cdots & 0 & 0 & T^{\rm FM} & H_{\rm 2d}^{\rm FM}(\mathbf{k}) & \cdots & 0 & 0 \\
\vdots & \vdots & \ddots & \vdots & \vdots & \vdots & \vdots & \ddots & \vdots & \vdots \\
0 & 0 & \cdots & 0 & 0 & 0 & 0 & \cdots & H_{\rm 2d}^{\rm FM}(\mathbf{k}) & T^{\rm FM\dagger} \\
0 & 0 & \cdots & 0 & 0 & 0 & 0 & \cdots & T^{\rm FM} & H_{\rm 2d}^{\rm FM}(\mathbf{k})
\end{array}\right), \tag{A1}$$

where $H_{\rm 2d}^{\rm NM(FM)}(\mathbf{k})$ is the Hamiltonian for a two-dimensional NM(FM) layer, $T^{\rm NM(FM)}$ is the hopping between nearest NM(FM) layers, and $T_{\rm int}$ is the interface hopping between the last NM layer ($z = N_{\rm NM}$) and the first FM layer ($z = N_{\rm NM} + 1$).

1. NM

We assume the NM hosts sp_α ($\alpha = x, y, z$) orbitals at each site, which was introduced in Ref. [23]. Writing the Hamiltonian in a finite film structure is straightforward as follows. The Hamiltonian within each two-dimensional NM layer consists of the spin-independent interaction and the SOC terms:

$$H_{\rm 2d}^{\rm NM}(\mathbf{k}) = H_{\rm 2d(0)}^{\rm NM}(\mathbf{k}) + H_{\rm so}^{\rm NM}(\mathbf{k}). \tag{A2}$$

First, the spin-independent interaction term contains the onsite energies and nearest-neighbor hoppings in the

plane:

$$H^{\mathrm{NM}}_{\mathrm{2d(0)}}(\mathbf{k}) = \begin{pmatrix} E_s(\mathbf{k}) & 2i\gamma_{sp}\sin(k_x a) & 2i\gamma_{sp}\sin(k_y a) & 0 \\ -2i\gamma_{sp}\sin(k_x a) & E_{p_x}(\mathbf{k}) & 0 & 0 \\ -2i\gamma_{sp}\sin(k_y a) & 0 & E_{p_y}(\mathbf{k}) & 0 \\ 0 & 0 & 0 & E_{p_z}(\mathbf{k}) \end{pmatrix} \otimes \mathrm{I}_{2\times 2}, \tag{A3}$$

where

$$E_s(\mathbf{k}) = E_s - 2t_s[\cos(k_x a) + \cos(k_y a)], \tag{A4a}$$
$$E_{p_x}(\mathbf{k}) = E_{p_x} + 2t_{p\sigma}\cos(k_x a) - 2t_{p\pi}\cos(k_y a), \tag{A4b}$$
$$E_{p_y}(\mathbf{k}) = E_{p_y} - 2t_{p\pi}\cos(k_x a) + 2t_{p\sigma}\cos(k_y a), \tag{A4c}$$
$$E_{p_z}(\mathbf{k}) = E_{p_z} - 2t_{p\pi}[\cos(k_x a) + \cos(k_y a)], \tag{A4d}$$

and $\mathrm{I}_{2\times 2}$ is the identity operator in the spin space. Here the basis states are

$$|\varphi^{(z)}_{l\sigma\mathbf{k}}\rangle = \sum_{\mathbf{R}} e^{i\mathbf{k}\cdot\mathbf{R}} |\phi^{(z)}_{l\sigma\mathbf{R}}\rangle, \tag{A5}$$

where $|\phi^{(z)}_{l\sigma\mathbf{R}}\rangle$ is a Wannier function localized at the Bravais lattice $\mathbf{R} = (R_x, R_y)$ with its orbital character $l = s, p_x, p_y, p_z$ and spin σ, which is defined in a layer located at z. For the Wannier states, E_s, E_{p_α} are onsite energies for s and p_α orbitals, and t_s, $t_{p\sigma(\pi)}$, γ_{sp} are the nearest hopping amplitudes between s orbitals, between p orbitals via $\sigma(\pi)$ bonding, and between s and p orbitals, respectively. Second, the SOC part is

$$H^{\mathrm{NM}}_{\mathrm{so}} = \frac{\alpha^{\mathrm{NM}}_{\mathrm{so}}}{\hbar^2}\mathbf{L}^{(p)}\cdot\mathbf{S}, \tag{A6}$$

where $\mathbf{S}$ is the spin operator and $\mathbf{L}^{(p)}$ is the OAM operator in p orbital space. Here $\alpha^{\mathrm{NM}}_{\mathrm{so}} > 0$ is the strength of the SOC in the NM. The OAM operator is explicitly expressed in a matrix representation

$$L^{(p)}_x = \hbar\begin{pmatrix} 0 & 0 & 0 \\ 0 & 0 & -i \\ 0 & i & 0 \end{pmatrix}, \tag{A7a}$$
$$L^{(p)}_y = \hbar\begin{pmatrix} 0 & 0 & i \\ 0 & 0 & 0 \\ -i & 0 & 0 \end{pmatrix}, \tag{A7b}$$
$$L^{(p)}_z = \hbar\begin{pmatrix} 0 & -i & 0 \\ i & 0 & 0 \\ 0 & 0 & 0 \end{pmatrix}, \tag{A7c}$$

with p_x, p_y, and p_z orbital Wannier functions as basis states. Finally, the interlayer coupling between neighboring NM layers is described as

$$T^{\mathrm{NM}} = \begin{pmatrix} -t_{ss} & 0 & 0 & -\gamma_{sp} \\ 0 & -t_{p\pi} & 0 & 0 \\ 0 & 0 & -t_{p\pi} & 0 \\ \gamma_{sp} & 0 & 0 & t_{p\sigma} \end{pmatrix} \otimes \mathrm{I}_{2\times 2}, \tag{A8}$$

where the basis states for the row and column are $\langle\varphi^{(z+1)}_{l\sigma\mathbf{k}}|$ and $|\varphi^{(z)}_{l'\sigma'\mathbf{k}}\rangle$, respectively, for $z = 1, \ldots, N_{\mathrm{NM}} - 1$.

2. FM

In the FM, we assume there are d_β ($\beta = xy, yz, zx, x^2 - y^2, z^2$) orbitals at each site. The Hamiltonian within each two-dimensional layer is

$$H^{\mathrm{FM}}_{\mathrm{2d}}(\mathbf{k}) = H^{\mathrm{FM}}_{\mathrm{2d(0)}}(\mathbf{k}) + H^{\mathrm{FM}}_{\mathrm{so}} + H^{\mathrm{FM}}_{\mathrm{xc}}, \tag{A9}$$

where each term describes the spin-independent interaction, SOC, and XC coupling with magnetization, respectively. The spin-independent interaction term includes onsite energies and nearest-neighbor hoppings in the plane:

$$H^{\mathrm{FM}}_{\mathrm{2d(0)}}(\mathbf{k}) = \begin{pmatrix} E_{d_{xy}}(\mathbf{k}) & 0 & 0 & 0 & 0 \\ 0 & E_{d_{yz}}(\mathbf{k}) & 0 & 0 & 0 \\ 0 & 0 & E_{d_{zx}}(\mathbf{k}) & 0 & 0 \\ 0 & 0 & 0 & E_{d_{x^2-y^2}}(\mathbf{k}) & 0 \\ 0 & 0 & 0 & 0 & E_{d_{z^2}}(\mathbf{k}) \end{pmatrix} \otimes \mathrm{I}_{2\times 2}, \tag{A10}$$

where

$$E_{d_{xy}}(\mathbf{k}) = E_{d_{xy}} + 2t_{d\pi}\cos(k_x a) + 2t_{d\pi}\cos(k_y a), \tag{A11a}$$
$$E_{d_{yz}}(\mathbf{k}) = E_{d_{yz}} - 2t_{d\delta}\cos(k_x a) + 2t_{d\pi}\cos(k_y a), \tag{A11b}$$
$$E_{d_{zx}}(\mathbf{k}) = E_{d_{zx}} + 2t_{d\pi}\cos(k_x a) - 2t_{d\delta}\cos(k_y a), \tag{A11c}$$
$$E_{d_{x^2-y^2}}(\mathbf{k}) = E_{d_{x^2-y^2}} - [(3/2)t_{d\sigma} + (1/2)t_{d\delta}] \times[\cos(k_x a) + \cos(k_y a)], \tag{A11d}$$
$$E_{d_{z^2}}(\mathbf{k}) = E_{d_{z^2}} - [(1/2)t_{d\sigma} + (3/2)t_{d\delta}] \times[\cos(k_x a) + \cos(k_y a)]. \tag{A11e}$$

Here E_{d_β} is the onsite energy of the d_β orbital, and $t_{d\sigma}, t_{d\pi}, t_{d\delta}$ are nearest-neighbor hoppings between d orbitals via σ, π, δ bondings, respectively. The basis states are defined similarly as Eq. (A5) but for d_β orbital Wannier functions. The SOC term is

$$H^{\mathrm{FM}}_{\mathrm{so}} = \frac{\alpha^{\mathrm{FM}}_{\mathrm{so}}}{\hbar^2}\mathbf{L}^{(d)}\cdot\mathbf{S}, \tag{A12}$$

where $\alpha^{\mathrm{FM}}_{\mathrm{so}} > 0$ is the SOC strength. Here $\mathbf{L}^{(d)}$ is the OAM operator in d orbital space, whose matrix representation is written as

$$L^{(d)}_x = \hbar\begin{pmatrix} 0 & 0 & -i & -i & -\sqrt{3}i \\ 0 & 0 & 0 & 0 & 0 \\ i & 0 & 0 & 0 & 0 \\ i & 0 & 0 & 0 & 0 \\ \sqrt{3}i & 0 & 0 & 0 & 0 \end{pmatrix}, \tag{A13a}$$

$$L_y^{(d)} = \hbar \begin{pmatrix} 0 & i & 0 & 0 & 0 \\ -i & 0 & 0 & 0 & 0 \\ 0 & 0 & 0 & -i & \sqrt{3}i \\ 0 & 0 & i & 0 & 0 \\ 0 & 0 & -\sqrt{3}i & 0 & 0 \end{pmatrix}, \quad \text{(A13b)}$$

$$L_z^{(d)} = \hbar \begin{pmatrix} 0 & 0 & 0 & 2i & 0 \\ 0 & 0 & i & 0 & 0 \\ 0 & -i & 0 & 0 & 0 \\ -2i & 0 & 0 & 0 & 0 \\ 0 & 0 & 0 & 0 & 0 \end{pmatrix}, \quad \text{(A13c)}$$

where the basis states are d_{xy}, d_{yz}, d_{zx}, $d_{x^2-y^2}$, d_{z^2} orbital Wannier functions. The XC interaction is

$$H_{\rm xc}^{\rm FM} = \frac{J}{\hbar}\hat{\mathbf{M}} \cdot \mathbf{S}, \quad \text{(A14)}$$

where $J > 0$ is the strength of the XC coupling, and $\hat{\mathbf{M}}$ is the direction of the magnetization. We assume $\hat{\mathbf{M}} = \hat{\mathbf{z}}$ in the calculation. The interlayer coupling between neighboring atomic layers of the FM is

$$T^{\rm FM} = \begin{pmatrix} -t_{d\delta} & 0 & 0 & 0 & 0 \\ 0 & t_{d\pi} & 0 & 0 & 0 \\ 0 & 0 & t_{d\pi} & 0 & 0 \\ 0 & 0 & 0 & -t_{d\delta} & 0 \\ 0 & 0 & 0 & 0 & -t_{d\sigma} \end{pmatrix} \otimes \mathrm{I}_{2\times 2}, \quad \text{(A15)}$$

where the basis for the row and column are $\langle \varphi_{l\sigma\mathbf{k}}^{(z+1)}|$ and $|\varphi_{l'\sigma'\mathbf{k}}^{(z)}\rangle$, respectively, for $z = N_{\rm NM}+1, \ldots, N_{\rm NM}+N_{\rm FM}-1$.

3. Interface

At the interface, there are hoppings between the last NM layer ($z = N_{\rm NM}$) and the first FM layer ($z = N_{\rm NM}+1$), which are expressed in

$$T_{\rm int} = \begin{pmatrix} 0 & 0 & 0 & 0 \\ 0 & 0 & \gamma_{pd\pi} & 0 \\ 0 & \gamma_{pd\pi} & 0 & 0 \\ 0 & 0 & 0 & 0 \\ 0 & 0 & 0 & -\gamma_{pd\sigma} \end{pmatrix} \otimes \mathrm{I}_{2\times 2}, \quad \text{(A16)}$$

where the basis for the row and column are $\langle \varphi_{l\sigma\mathbf{k}}^{(N_{\rm NM}+1)}|$ and $|\varphi_{l'\sigma'\mathbf{k}}^{(N_{\rm NM})}\rangle$, respectively. Here $\gamma_{pd\sigma(\pi)}$ is the nearest-neighbor hopping between p and d orbitals via $\sigma(\pi)$ hoppings. We neglect the hopping from a s orbital in the NM to d orbitals in the FM, since the s orbital does not carry the OAM, thus not affecting the orbital injection.

4. Parameter setting

For the tight-binding model defined above, parameters which we used for the calculation in Figs. 2, 3, and 4(a) are set as

$$E_s = 3.2, \quad \text{(A17a)}$$
$$E_{p_x} = E_{p_y} = E_{p_z} = -0.5, \quad \text{(A17b)}$$
$$t_s = 0.5, \quad \text{(A17c)}$$
$$t_{p\sigma} = 0.5, \quad \text{(A17d)}$$
$$t_{p\pi} = 0.2, \quad \text{(A17e)}$$
$$\gamma_{sp} = 0.5, \quad \text{(A17f)}$$
$$\alpha_{\rm so}^{\rm NM} = 0, \quad \text{(A17g)}$$

for the NM,

$$E_{d_{xy}} = E_{d_{yz}} = E_{d_{zx}} = E_{d_{x^2-y^2}} = E_{d_{z^2}} = -0.5, \quad \text{(A18a)}$$
$$t_{d\sigma} = 0.1, \quad \text{(A18b)}$$
$$t_{d\pi} = 0.05, \quad \text{(A18c)}$$
$$t_{d\delta} = 0.02, \quad \text{(A18d)}$$
$$J = 0.5, \quad \text{(A18e)}$$
$$\alpha_{\rm so}^{\rm FM} = 0.1 \quad \text{(A18f)}$$

for the FM, and

$$\gamma_{pd\sigma} = 0.4, \quad \text{(A19a)}$$
$$\gamma_{pd\pi} = 0.1 \quad \text{(A19b)}$$

for the interface. All parameters are expressed in unit of eV. For the calculation of Fig. 4(b), we tune the magnitude of $\alpha_{\rm so}^{\rm FM}$ while keeping the other parameters unchanged.

APPENDIX B: ROLE OF THE INTERFACIAL HOPPINGS ON THE ORBITAL INJECTION

For the injection of the OAM across the interface, interfacial hoppings should occur such that a coherent superposition,

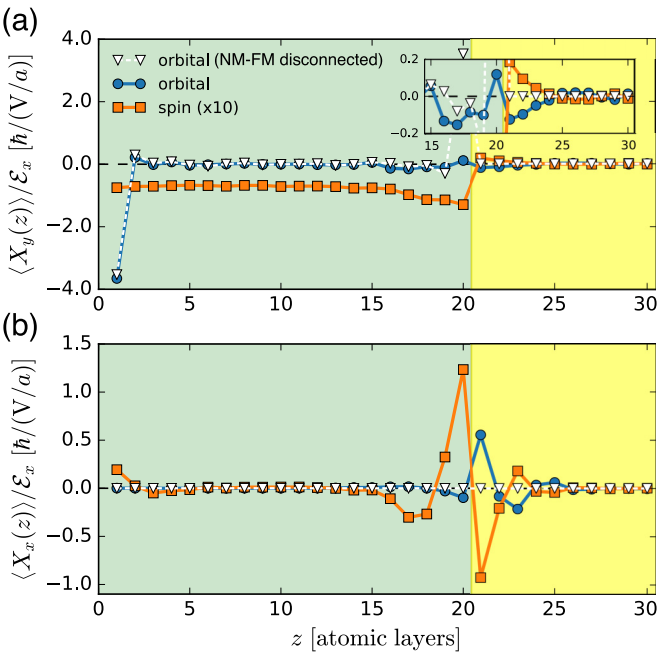

FIG. 5. (a) $\langle X_y(z)\rangle/\mathcal{E}_x$ and (b) $\langle X_x(z)\rangle/\mathcal{E}_x$ as a function of z for $E_{\rm F} = -0.9$ eV, when the relative sign of the interface hoppings is flipped [Eq. (B1)]. Blue circles (orange squares) depict the orbital (spin multiplied by factor 10) accumulation profile in the NM ($1 \leqslant z \leqslant 20$) and the FM ($21 \leqslant z \leqslant 30$). White inverted triangles depict the orbital accumulation profile when the NM and FM are disconnected. The inset in (a) presents a magnified plot near the NM/FM interface.

which carries finite OAM, is maintained during the injection. Thus, the relative sign of $\gamma_{pd\sigma}$ and $\gamma_{pd\pi}$ in Eq. (13) is crucial, by which the OT changes the sign. In the tight-binding model used in the paper, we assume the positive sign for both $\gamma_{pd\sigma}$ and $\gamma_{pd\pi}$ [Eq. (A19)]. In order to demonstrate that the interfacial hoppings are critical for the injection of the OAM, we present calculation results for $\langle X_y(z)\rangle/\mathcal{E}_x$ and $\langle X_x(z)\rangle/\mathcal{E}_x$ in Figs. 5(a) and 5(b), respectively, by assuming

$$\gamma_{pd\sigma} = -0.4, \tag{B1a}$$

$$\gamma_{pd\pi} = 0.1, \tag{B1b}$$

which is to be compared with Fig. 3. We find that $\langle L_y(z)\rangle/\mathcal{E}_x$ is unchanged near $z = 1$, which is away from the interface. However, near the interface ($z = 20$) and in the FM region ($21 \leqslant z \leqslant 30$), the sign of the $\langle L_y(z)\rangle/\mathcal{E}_x$ in Fig. 5(a) is opposite to that in Fig. 3(b). As a consequence, $\langle S_y(z)\rangle/\mathcal{E}_x$, which is induced by the SOC and the injected OAM, also changes the sign [Fig. 5(a)]. Since $\langle S_x(z)\rangle/\mathcal{E}_x$ precesses along the magnetization by the XC interaction and $\langle L_x(z)\rangle/\mathcal{E}_x$ follows by the SOC in the FM, the signs of $\langle L_x(z)\rangle/\mathcal{E}_x$ and $\langle S_x(z)\rangle/\mathcal{E}_x$ in Fig. 5(b) are flipped compared to Fig. 3(c).

This result implies that when the interfacial hoppings such as Eq. (13) become randomized, i.e., by the intermixing, the injection efficiency for the OAM is significantly reduced. This is a key characteristic of the orbital injection mechanism, which does not have a counterpart in the spin injection mechanism. We remark that spin injection efficiency is not affected by the interfacial disorders unless the SOC is significant. Therefore, the orbital transparency is expected to be much more susceptible to the interface crystallinity than the spin transparency. This can be a way to distinguish the OT from the ST.

[1] I. M. Miron, K. Garello, G. Gaudin, P.-J. Zermatten, M. V. Costache, S. Auffret, S. Bandiera, B. Rodmacq, A. Schuhl, and P. Gambardella, Perpendicular switching of a single ferromagnetic layer induced by in-plane current injection, Nature (London) **476**, 189 (2011).

[2] L. Liu, O. J. Lee, T. J. Gudmundsen, D. C. Ralph, and R. A. Buhrman, Current-Induced Switching of Perpendicularly Magnetized Magnetic Layers Using Spin Torque from the Spin Hall Effect, Phys. Rev. Lett. **109**, 096602 (2012).

[3] L. Liu, C.-F. Pai, Y. Li, H. W. Tseng, D. C. Ralph, and R. A. Buhrman, Spin-torque switching with the giant spin Hall effect of tantalum, Science **336**, 555 (2012).

[4] G. Yu, P. Upadhyaya, Y. Fan, J. G. Alzate, W. Jiang, K. L. Wong, S. Takei, S. A. Bender, L.-T. Chang, Y. Jiang, M. Lang, J. Tang, Y. Wang, Y. Tserkovnyak, P. K. Amiri, and K. L. Wang, Switching of perpendicular magnetization by spin-orbit torques in the absence of external magnetic fields, Nat. Nanotech. **9**, 548 (2014).

[5] K. Garello, C. O. Avci, I. M. Miron, M. Baumgartner, A. Ghosh, S. Auffret, O. Boulle, G. Gaudin, and P. Gambardella, Ultrafast magnetization switching by spin-orbit torques, Appl. Phys. Lett. **105**, 212402 (2014).

[6] I. M. Miron, T. Moore, H. Szambolics, L. D. Buda-Prejbeanu, S. Auffret, B. Rodmacq, S. Pizzini, J. Vogel, M. Bonfim, A. Schuhl, and G. Gaudin, Fast current-induced domain-wall motion controlled by the Rashba effect, Nat. Mater. **10**, 419 (2011).

[7] K.-S. Ryu, L. Thomas, S.-H. Yang, and S. Parkin, Chiral spin torque at magnetic domain walls, Nat. Nanotech. **8**, 527 (2013).

[8] S. Emori, U. Bauer, S.-M. Ahn, E. Martinez, and G. S. D. Beach, Current-driven dynamics of chiral ferromagnetic domain walls, Nat. Mater. **12**, 611 (2013).

[9] E. Martinez, S. Emori, and G. S. D. Beach, Current-driven domain wall motion along high perpendicular anisotropy multilayers: The role of the Rashba field, the spin Hall effect, and the Dzyaloshinskii-Moriya interaction, Appl. Phys. Lett. **103**, 072406 (2013).

[10] U. H. Pi, K. Won Kim, J. Y. Bae, S. C. Lee, Y. J. Cho, K. S. Kim, and S. Seo, Tilting of the spin orientation induced by Rashba effect in ferromagnetic metal layer, Appl. Phys. Lett. **97**, 162507 (2010).

[11] I. Mihai Miron, G. Gaudin, S. Auffret, B. Rodmacq, A. Schuhl, S. Pizzini, J. Vogel, and P. Gambardella, Current-driven spin torque induced by the Rashba effect in a ferromagnetic metal layer, Nat. Mater. **9**, 230 (2010).

[12] C.-F. Pai, L. Liu, Y. Li, H. W. Tseng, D. C. Ralph, and R. A. Buhrman, Spin transfer torque devices utilizing the giant spin Hall effect of tungsten, Appl. Phys. Lett. **101**, 122404 (2012).

[13] K.-W. Kim, S.-M. Seo, J. Ryu, K.-J. Lee, and H.-W. Lee, Magnetization dynamics induced by in-plane currents in ultrathin magnetic nanostructures with Rashba spin-orbit coupling, Phys. Rev. B **85**, 180404(R) (2012).

[14] P. M. Haney, H.-W. Lee, K.-J. Lee, A. Manchon, and M. D. Stiles, Current induced torques and interfacial spin-orbit coupling: Semiclassical modeling, Phys. Rev. B **87**, 174411 (2013).

[15] P. M. Haney, H.-W. Lee, K.-J. Lee, A. Manchon, and M. D. Stiles, Current-induced torques and interfacial spin-orbit coupling, Phys. Rev. B **88**, 214417 (2013).

[16] H. Kurebayashi, J. Sinova, D. Fang, A. C. Irvine, T. D. Skinner, J. Wunderlich, V. Novák, R. P. Campion, B. L. Gallagher, E. K. Vehstedt, L. P. Zârbo, K. Výborný, A. J. Ferguson, and T. Jungwirth, An antidamping spin-orbit torque originating from the Berry curvature, Nat. Nanotech. **9**, 211 (2014).

[17] M. Hayashi, J. Kim, M. Yamanouchi, and H. Ohno, Quantitative characterization of the spin-orbit torque using harmonic Hall voltage measurements, Phys. Rev. B **89**, 144425 (2014).

[18] F. Freimuth, S. Blügel, and Y. Mokrousov, Spin-orbit torques in Co/Pt(111) and Mn/W(001) magnetic bilayers from first principles, Phys. Rev. B **90**, 174423 (2014).

[19] K.-W. Kim, K.-J. Lee, J. Sinova, H.-W. Lee, and M. D. Stiles, Spin-orbit torques from interfacial spin-orbit coupling for various interfaces, Phys. Rev. B **96**, 104438 (2017).

[20] F. Mahfouzi and N. Kioussis, First-principles study of the angular dependence of the spin-orbit torque in Pt/Co and Pd/Co bilayers, Phys. Rev. B **97**, 224426 (2018).

[21] T. Tanaka, H. Kontani, M. Naito, T. Naito, D. S. Hirashima, K. Yamada, and J. Inoue, Intrinsic spin Hall effect and orbital Hall effect in 4*d* and 5*d* transition metals, Phys. Rev. B **77**, 165117 (2008).

[22] H. Kontani, T. Tanaka, D. S. Hirashima, K. Yamada, and J. Inoue, Giant Orbital Hall Effect in Transition Metals: Origin of Large Spin and Anomalous Hall Effects, Phys. Rev. Lett. **102**, 016601 (2009).

[23] D. Go, D. Jo, C. Kim, and H.-W. Lee, Intrinsic Spin and Orbital Hall Effects from Orbital Texture, Phys. Rev. Lett. **121**, 086602 (2018).

[24] D. Jo, D. Go, and H.-W. Lee, Gigantic intrinsic orbital Hall effects in weakly spin-orbit coupled metals, Phys. Rev. B **98**, 214405 (2018).

[25] S. R. Park, C. H. Kim, J. Yu, J. H. Han, and C. Kim, Orbital-Angular-Momentum Based Origin of Rashba-Type Surface Band Splitting, Phys. Rev. Lett. **107**, 156803 (2011).

[26] J.-H. Park, C. H. Kim, H.-W. Lee, and J. H. Han, Orbital chirality and Rashba interaction in magnetic bands, Phys. Rev. B **87**, 041301(R) (2013).

[27] S. R. Park and C. Kim, Microscopic mechanism for the Rashba spin-band splitting: Perspective from formation of local orbital angular momentum, J. Electron. Spectrosc. Relat. Phenom. **201**, 6 (2015).

[28] T. Yoda, T. Yokoyama, and S. Murakami, Current-induced orbital and spin magnetizations in crystals with helical structure, Sci. Rep. **5**, 12024 (2015).

[29] D. Go, J.-P. Hanke, P. M. Buhl, F. Freimuth, G. Bihlmayer, H.-W. Lee, Y. Mokrousov, and S. Blügel, Toward surface orbitronics: Giant orbital magnetism from the orbital Rashba effect at the surface of sp-metals, Sci. Rep. **7**, 46742 (2017).

[30] L. Salemi, M. Berritta, A. K. Nandy, and P. M. Oppeneer, Orbitally dominated Rashba-Edelstein effect in noncentrosymmetric antiferromagnets, Nat. Commun. **10**, 5381 (2019).

[31] V. Sunko, H. Rosner, P. Kushwaha, S. Khim, F. Mazzola, L. Bawden, O. J. Clark, J. M. Riley, D. Kasinathan, M. W. Haverkort, T. K. Kim, M. Hoesch, J. Fujii, I. Vobornik, A. P. Mackenzie, and P. D. C. King, Maximal Rashba-like spin splitting via kinetic-energy-coupled inversion-symmetry breaking, Nature (London) **549**, 492 (2017).

[32] C. S. Wang and J. Callaway, Band structure of nickel: Spin-orbit coupling, the Fermi surface, and the optical conductivity, Phys. Rev. B **9**, 4897 (1974).

[33] L. Zhu, D. C. Ralph, and R. A. Buhrman, Highly efficient spin-current generation by the spin Hall effect in $Au_{1-x}Pt_x$, Phys. Rev. Appl. **10**, 031001 (2018).

[34] Y. Du, S. Karube, H. Gamou, J. Ryu, S. Takahashi, M. Kohda, and J. Nitta, Anomalous spin orbit torques with large Rashba spin orbit coupling in epitaxial Pt/Co bilayers, arXiv:1807.10867.

[35] V. P. Amin, J. Li, M. D. Stiles, and P. M. Haney, Intrinsic spin currents in ferromagnets, Phys. Rev. B **99**, 220405(R) (2019).

[36] W. Wang, T. Wang, V. P. Amin, Y. Wang, A. Radhakrishnan, A. Davidson, S. R. Allen, T. J. Silva, H. Ohldag, D. Balzar, B. L. Zink, P. M. Haney, J. Q. Xiao, D. G. Cahill, V. O. Lorenz, and X. Fan, Anomalous spin-orbit torques in magnetic single-layer films, Nat. Nanotech. **14**, 819 (2019).

[37] Z. C. Zheng, Q. X. Guo, D. Jo, D. Go, L. H. Wang, H. C. Chen, W. Yin, X. M. Wang, G. H. Yu, W. He, H.-W. Lee, J. Teng, and T. Zhu, Magnetization switching driven by current-induced torque from weakly spin-orbit coupled Zr, Phys. Rev. Res. **2**, 013127 (2020).

[38] C. Du, H. Wang, F. Yang, and P. C. Hammel, Systematic variation of spin-orbit coupling with d-orbital filling: Large inverse spin Hall effect in 3d transition metals, Phys. Rev. B **90**, 140407(R) (2014).

[39] D. Qu, S. Y. Huang, and C. L. Chien, Inverse spin Hall effect in Cr: Independence of antiferromagnetic ordering, Phys. Rev. B **92**, 020418(R) (2015).

[40] B. F. Miao, S. Y. Huang, D. Qu, and C. L. Chien, Inverse Spin Hall Effect in a Ferromagnetic Metal, Phys. Rev. Lett. **111**, 066602 (2013).

[41] A. Tsukahara, Y. Ando, Y. Kitamura, H. Emoto, E. Shikoh, M. P. Delmo, T. Shinjo, and M. Shiraishi, Self-induced inverse spin Hall effect in permalloy at room temperature, Phys. Rev. B **89**, 235317 (2014).

[42] L. Wollmann, A. K. Nayak, S. S. Parkin, and C. Felser, Heusler 4.0: Tunable materials, Annu. Rev. Mater. Res. **47**, 247 (2017).

[43] Y.-C. Lau, H. Lee, G. Qu, K. Nakamura, and M. Hayashi, Spin Hall effect from hybridized 3d−4p orbitals, Phys. Rev. B **99**, 064410 (2019).

[44] We performed self-consistent density functional theory calculations for the electronic structure of B2-CoGa by using FLEUR code [49], which implements the full-potential linearized augmented planewave [50]. Exchange and correlation effects were treated within the generalized gradient approximation [51]. In the simple cubic structure, the lattice constant was chosen to be $a = 5.42a_0$ following Ref. [43], where a_0 is the Bohr radius. The muffin-tin radii of Co and Ga were chosen as $2.30a_0$ for both. The plane-wave cutoff was chosen as $K_{\max} = 3.40a_0^{-1}$, and the Monkhorst-Pack $\mathbf{k}$ points of $16 \times 16 \times 16$ were sampled from the first Brillouin zone. The SOC was included self-consistently within the second-variation scheme. Based on the converged charge density, maximally localized Wannier functions (MLWFs) were obtained. Starting from 26 trial Wannier functions (s, p, d orbitals for Co and s, p orbitals for Ga, respectively), we obtained MLWFs out of 52 Bloch states by using WANNIER90 code [52]. The frozen window for the disentanglement was set 5.0 eV above the Fermi energy. The matrix representations of the Hamiltonian, spin, and orbital operators were obtained from the MLWF as basis states. Then the OHC and SHC were calculated from the Kubo formula on the interpolated $\mathbf{k}$-point meshgrid ($240 \times 240 \times 240$) in the first Brillouin zone.

[45] L. M. Canonico, T. P. Cysne, T. G. Rappoport, and R. B. Muniz, Two-dimensional orbital Hall insulators, arXiv:1908.00927.

[46] L. M. Canonico, T. P. Cysne, A. Molina-Sanchez, R. B. Muniz, and T. G. Rappoport, Orbital Hall insulating phase in transition metal dichalcogenide monolayers, arXiv:2001.03592.

[47] X. Chen, Y. Liu, G. Yang, H. Shi, C. Hu, M. Li, and H. Zeng, Giant antidamping orbital torque originating from the orbital Rashba-Edelstein effect in ferromagnetic heterostructures, Nat. Commun. **9**, 2569 (2018).

[48] S. Emori, T. Nan, A. M. Belkessam, X. Wang, A. D. Matyushov, C. J. Babroski, Y. Gao, H. Lin, and N. X. Sun, Interfacial spin-orbit torque without bulk spin-orbit coupling, Phys. Rev. B **93**, 180402(R) (2016).

[49] https://www.flapw.de.

[50] E. Wimmer, H. Krakauer, M. Weinert, and A. J. Freeman, Full-potential self-consistent linearized-augmented-plane-wave method for calculating the electronic structure of molecules and surfaces: O_2 molecule, Phys. Rev. B **24**, 864 (1981).

[51] J. P. Perdew, K. Burke, and M. Ernzerhof, Generalized Gradient Approximation Made Simple, Phys. Rev. Lett. **77**, 3865 (1996).

[52] G. Pizzi, V. Vitale, R. Arita, S. Blügel, F. Freimuth, G. Géranton, M. Gibertini, D. Gresch, C. Johnson, T. Koretsune, J. Ibañez-Azpiroz, H. Lee, J.-M. Lihm, D. Marchand, A. Marrazzo, Y. Mokrousov, J. I. Mustafa, Y. Nohara, Y. Nomura, L. Paulatto, S. Poncé, T. Ponweiser, J. Qiao, F. Thöle, S. S. Tsirkin, M. Wierzbowska, N. Marzari, D. Vanderbilt, I. Souza, A. A. Mostofi, and J. R. Yates, Wannier90 as a community code: New features and applications, J. Phys. Cond. Matt. **32**, 165902 (2020).